Radar-Camera Extended Kalman Filter for Robust Small UAV 3D Trajectory Estimation

Christopher Grebe [1]

***Abstract*— This work implements a trajectory estimation system for objects in 3D space utilizing a 2D automotive grade radar system and common camera. The work includes data association, trajectory estimation and outlier rejection. The application focus of this work is the trajectory estimation of unwanted unmanned aerial vehicles (UAVs) which makes motion information from the target being tracked unavailable. This increases the dependance of the system on effective data association and outlier rejection. The estimation methodology must be compatible with the non-linear nature of the problem. For this reason the extended Kalman filter (EKF) is chosen due to its computational efficiency and a gating region is established from the prediction of the EKF allowing for a global nearest neighbour (GNN) data association approach to be applied. Lastly outlier rejection is performed using a dynamic innovation saturation method.**

A presentation of results is available at Video Results.

I. Introduction

The availability of UAVs to the general public has significantly increased over recent years. People use UAVs for a range of activities such as photography and recreation. Despite their benefits and capabilities, UAVs have the potential to pose a threat to areas such as prisons where UAVs are utilized to smuggle drugs and phones to inmates and high security areas where UAVs may be used to transport and detonate explosives. UAVs also have the potential to harm the general public when they are flown over large crowds at outdoor events and upon collision with commercial aircrafts in an airport setting.

Significant recent attention has been brought to the effective trajectory estimation of UAVs in 3D space. Various sensors such as radar, acoustic, camera and LiDAR have been applied to problem of UAV trajectory estimation. One method often used for UAV detection in prison environments is radio frequency (RF) detection. Despite advancements in RF-based UAV localization, these systems inherently rely on the UAV communicating with a ground station which does not occur with autonomous UAVs [1]. Work in [2] is able to estimate UAV pose with six degrees-of-freedom using cameras set up throughout a confined space. However, for UAV tracking in large open spaces cameras are not ideal due to their lack of depth information when utilized without a range providing sensor. Work in [3] conducts UAV detection with a standard automotive LiDAR sensor. Poor resolution at range leads to the inability of current LiDAR solutions to provide sufficient return information for effective UAV trajectory estimation. [3] proposes a panning LiDAR system with a extremely narrow field of view (FOV) and high laser power to perform effective UAV detection at kilometre ranges. However, this combination of narrow FOV and high laser power makes the system not compliant with Class 1 laser safety standards required for operation in open public environments.

In the current airport setting, long range radar systems are commonly employed for monitoring of air traffic. These systems are unable to detect UAVs as the typical pulse widths utilized to allow for kilometre detection cause the minimum detection range to be approximately 250m for the average system. Advancements in radar technology for automotive applications has resulted in significant reduction in price of millimetre wave radar systems. These systems overcome the problems associated with longer wavelength radar systems typically found at airports. The capabilities of automotive radar systems for trajectory estimation of UAVs will be evaluated in this work.

In addition to an adequate sensor, effective trajectory estimation must be performed for a complete UAV tracking solution. This estimation problem is non-linear in nature and will therefore require a solution which can account for non-linearities. Two common methods for trajectory estimation with non-linear systems are the extended Kalman filter (EKF) and the sigma point Kalman filter. The EKF involves linearization through first-order derivative. It is a computationally effective method, but has the possibility of corruption of the posterior mean and covariance. In contrast, the sigma point Kalman filter preserves the mean and covariance. One implementation of the sigma point Kalman filter is the unscented Kalman filter which involves selection sigma points which preserve the mean and covariance of the prior, passing the sigma points through the non-linearity and calculating the posterior mean and covariance from the points passed through the non-linearity [4].

We hypothesize that a 2D radar sensor ground station can be effectively utilized with a single camera to perform trajectory estimation of an UAV in 3D space without any communication with the UAV. This work provides a preliminary evaluation of UAV trajectory estimation through the use of a reflective radar target in place of a UAV. Thus we will seek to determine if trajectory estimation is possible for an idealized target. For this work it is assumed that the target remains within the FOV of both the single radar and camera. This project will therefore not aim to solve issues related to FOV coverage by multiple ground stations.

[1]Christopher Grebe is with the University of Toronto Institute for Aerospace Studeis, Toronto, Canada christopher.grebe@robotics.utias.utoronto.ca

Results obtained show that a radar-camera ground station can be utilized to estimate the trajectory of an object in 3D space if the input data-stream is consistent enough to perform effective data association. The significant noise presence in radar data makes association difficult as any inconsistency in the radar data may lead to a divergence of the estimated trajectory. Overall, this work has the potential to provide proof of concept for a cost effective UAV trajectory estimation system.

This paper is organized into two main categories. First, in the methodology section of the paper the problem will be formulated in detail and the process used to solve the problem will be discussed and supported. Second, in the results section of the paper, both simulation and experimental results will be presented and reviewed.

II. Methodology

The first task presented in any estimation problem is to define the states that will be estimated.

$$\begin{bmatrix} x_k & y_k & z_k & \dot{x}_k & \dot{y}_k & \dot{z}_k \end{bmatrix}^T \tag{1}$$

In this work the cartesian coordinates and velocity of the target are estimated in three dimensions. The motion of these states is defined using the constant velocity motion model according to 2.

$$\underbrace{\begin{bmatrix} x_k \\ y_k \\ z_k \\ \dot{x}_k \\ \dot{y}_k \\ \dot{z}_k \end{bmatrix}}_{(\mathbf{x}_k)} = \underbrace{\begin{bmatrix} \mathbf{I}_{(3\times3)} & \begin{matrix} T & & \\ & T & \\ & & T \end{matrix} \\ & \mathbf{I}_{(3\times3)} \end{bmatrix}}_{(\mathbf{A})} \begin{bmatrix} x_{k-1} \\ y_{k-1} \\ z_{k-1} \\ \dot{x}_{k-1} \\ \dot{y}_{k-1} \\ \dot{z}_{k-1} \end{bmatrix} + \mathbf{w}_k \tag{2}$$

Where T is the time interval and $\mathbf{w}_k$ is the process noise. The estimated states in this work are statistically dependant upon each other and as a result the process noise covariance matrix $\mathbf{Q}_k$ will reflect this.

$$\mathbf{w}_k \sim \mathcal{N}(\mathbf{0}, \mathbf{Q}_k) \tag{3}$$

The process noise covariance for the constant velocity motion model can be obtained via Equation 4 as shown in [5].

$$\mathbf{Q}_k = E[\mathbf{w}_k \mathbf{w}_k^T] \tag{4}$$

$$\mathbf{Q}_k = q \begin{bmatrix} \frac{T^3}{3} & 0 & 0 & \frac{T^2}{2} & 0 & 0 \\ 0 & \frac{T^3}{3} & 0 & 0 & \frac{T^2}{2} & 0 \\ 0 & 0 & \frac{T^3}{3} & 0 & 0 & \frac{T^2}{2} \\ \frac{T^2}{2} & 0 & 0 & T & 0 & 0 \\ 0 & \frac{T^2}{2} & 0 & 0 & T & 0 \\ 0 & 0 & \frac{T^2}{2} & 0 & 0 & T \end{bmatrix} \tag{5}$$

where q is a constant scaling factor.

We begin creating our observation model by establishing that the single radar sensor solution is insufficient. The defining observation model for a radar only system is Equation 6.

$$\underbrace{\begin{bmatrix} R_k \\ A_k \\ \dot{R}_k \end{bmatrix}}_{(\mathbf{y}_k)} = \begin{bmatrix} \sqrt{[x_k, y_k, z_k][x_k, y_k, z_k]} \\ \arctan(\frac{y_k}{x_k}) \\ \frac{[x_k, y_k, z_k][\dot{x}_k, \dot{y}_k, \dot{z}_k]^T}{\sqrt{[x_k, y_k, z_k][x_k, y_k, z_k]}} \end{bmatrix} + \mathbf{n}_k \tag{6}$$

where $\mathbf{R}_k$ is range, $\mathbf{A}_k$ is Azimuth, $\dot{\mathbf{R}}_k$ is range rate and $\mathbf{n}_k$ is the measurement noise defined in Equation 7 as zero-mean with a covariance matrix $\mathbf{R}_k$.

$$\mathbf{n}_k \sim \mathcal{N}(\mathbf{0}, \mathbf{R}_k) \tag{7}$$

$$\mathbf{R}_k = \begin{bmatrix} \sigma_r^2 & & \\ & \sigma_\theta^2 & \\ & & \sigma_{\dot{r}}^2 \end{bmatrix} \tag{8}$$

Intuitively it can be seen that the radar only observation model will not be observable over the the six estimated states. This can be theoretically shown through the Fisher Information Matrix (FIM) [6]. The FIM is defined as

$$\begin{aligned} \mathbf{F}_\theta(X) &= \mathrm{COV}_\theta\{\nabla_\theta \ln[L_\theta(X)]\} \\ &= E_\theta\{\nabla_\theta \ln[L_\theta(X)] \nabla_\theta^T \ln[L_\theta(X)]\} \end{aligned} \tag{9}$$

where θ represents the observability parameters/system states, X is the measurement vector and $L_\theta(X)$ is the likelihood function of the observability parameters.

$$L_\theta(X) = p_X(X|\theta) \tag{10}$$

A system with zero-mean gaussian noise $\mathbf{n}_k$ and an invertible covariance matrix $\mathbf{R}$ has the FIM,

$$\mathbf{F}_\theta(X) = \nabla_\theta h(\theta) \mathbf{R}^{-1} \nabla_\theta^T h(\theta) \tag{11}$$

where $h()$ is the observation model of the system. Appendix IV-A theoretically proves that the observation model in Equation 6 is unobservable. Keeping cost effectiveness in mind, a single camera is chosen to capture additional state information. With the addition of a camera, the observation model will be defined according to Equation 12.

$$\underbrace{\begin{bmatrix} R_k \\ A_k \\ \dot{R}_k \\ u_k \\ v_k \end{bmatrix}}_{(\mathbf{y}_k)} = \begin{bmatrix} \sqrt{[x_k, y_k, z_k][x_k, y_k, z_k]} \\ \arctan(\frac{y_k}{x_k}) \\ \frac{[x_k, y_k, z_k][\dot{x}_k, \dot{y}_k, \dot{z}_k]^T}{\sqrt{[x_k, y_k, z_k][x_k, y_k, z_k]}} \\ f_u y_k / x_k \\ f_v z_k / x_k \end{bmatrix} + \mathbf{n}_k \tag{12}$$

where u_k and v_k are the horizontal and vertical pixels locations and f_u and f_v are the camera focal lengths in horizontal and vertical pixel coordinates. $\mathbf{n}_k$ is extended to include the camera measurement variance. It should also be noted that the notation of the camera portion of the observation model has been modified to fit the radar convention of x being downrange. To test the observability of the system the FIM is applied to the updated observation model. Appendix IV-B proves via the FIM, that even with the addition of a camera to the sensor suite, the system is still unobservable. However, the system can be shown to be locally weakly observable through the construction of an observability matrix from the gradients of the the Lie derivatives of our non-linear measurement model [7][8]. This proof is shown in Appendix IV-D. In addition, if the velocity states are removed from the set of estimated states, the radar-camera system is fully observable as shown in Appendix IV-C. Work will proceed with the radar-camera system as the 3D object location in space is observable despite the UAV motion not being fully observable.

The reference frames present in this system are shown in Figure 1. The radar and camera each have their own reference frames with some known transformation T_{ca} between them. For the observation model in Equation 12 we have defined the camera and radar reference frames identically meaning that the transformation matrix T_{cv} is the identity matrix. Additionally, the Vicon reference frame can be seen in Figure 1. The Vicon motion capture system will be discussed further in Section III-C as it will be utilized to provide ground truth information for evaluation of the experimental results obtained.

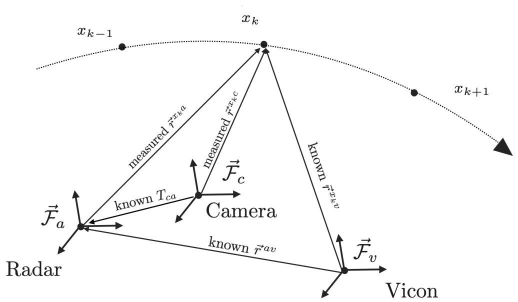

Fig. 1. Frame Diagram

Now that the problem motion and observation models have been defined, an appropriate trajectory estimation method can be applied to solve the estimation problem. Due to the non-linearity of the radar measurement model the extended Kalman filter (EKF) was utilized. The EKF offers computational benefits over other non-linear estimation methods so it is an ideal non-linear solution if it produces sufficiently accurate trajectory estimation for the task considered. The EKF is defined by the following equations [5]:

$$\check{\mathbf{P}}_k = \mathbf{F}_{k-1}\hat{\mathbf{P}}_{k-1}\mathbf{F}_{k-1}^T + \mathbf{Q}'_k \tag{13}$$

$$\check{\mathbf{x}} = \mathbf{f}(\hat{\mathbf{x}}_{k-1}, \mathbf{v}_k, \mathbf{0}) \tag{14}$$

$$\mathbf{K}_k = \check{\mathbf{P}}_k\mathbf{G}_k^T(\mathbf{G}_k\check{\mathbf{P}}_k\mathbf{G}_k^T + \mathbf{R}'_k)^{-1} \tag{15}$$

$$\hat{\mathbf{P}}_k = (\mathbf{1} - \mathbf{K}_k\mathbf{G}_k)\check{\mathbf{P}}_k \tag{16}$$

$$\hat{\mathbf{x}}_k = \check{\mathbf{x}}_k + \mathbf{K}_k(\mathbf{y}_k - \mathbf{g}(\check{\mathbf{x}}_k, \mathbf{0})) \tag{17}$$

where $\check{\mathbf{P}}_k$ is the predicted covariance matrix, $\check{\mathbf{x}}$ is the predicted state, $\mathbf{K}_k$ is the Kalman gain, $\hat{\mathbf{P}}_k$ is the estimated covariance matrix, $\hat{\mathbf{x}}_k$ is the estimated sate and $\mathbf{y}_k$ is the measurement. $\mathbf{F}_k$ and $\mathbf{G}_k$ are the linearization of the motion and observation models respectively as shown in Equation 18 and Equation 19.

$$\mathbf{f}(\mathbf{x}_{k-1}, \mathbf{v}_k, \mathbf{w}_k) \approx \check{\mathbf{x}}_k + \mathbf{F}_{k-1}(\mathbf{x}_{k-1} - \hat{\mathbf{x}}_{k-1}) + \mathbf{w}'_k \tag{18}$$

$$\mathbf{g}(\mathbf{x}_k, \mathbf{n}_k) \approx \check{\mathbf{y}}_k + \mathbf{G}_k(\mathbf{x}_k - \check{\mathbf{x}}_k) + \mathbf{n}'_k \tag{19}$$

where

$$\mathbf{F}_{k-1} = \frac{\partial \mathbf{f}(\mathbf{x}_{k-1}, \mathbf{v}_k, \mathbf{w}_k)}{\partial \mathbf{x}_{k-1}}\Big|_{\hat{\mathbf{x}}_{k-1}, \mathbf{v}_k, \mathbf{0}} \tag{20}$$

$$\frac{\partial \mathbf{f}(\mathbf{x}_{k-1}, \mathbf{v}_k, \mathbf{w}_k)}{\partial \mathbf{x}_{k-1}} = \begin{bmatrix} \mathbf{I}_{(3\times3)} & \begin{matrix} T & & \\ & T & \\ & & T \end{matrix} \\ & \mathbf{I}_{(3\times3)} \end{bmatrix} \tag{21}$$

$$\mathbf{D} = \frac{\partial \mathbf{f}(\mathbf{x}_{k-1}, \mathbf{v}_k, \mathbf{w}_k)}{\partial \mathbf{w}_k} = \mathbf{I}_{(6\times6)} \tag{22}$$

$$\mathbf{w}'_k = \frac{\partial \mathbf{f}(\mathbf{x}_{k-1}, \mathbf{v}_k, \mathbf{w}_k)}{\partial \mathbf{w}_k}\Big|_{\hat{\mathbf{x}}_{k-1}, \mathbf{v}_k, \mathbf{0}} \mathbf{w}_k \tag{23}$$

$$\mathbf{Q}' = \mathbf{D}\mathbf{Q}\mathbf{D}^T \tag{24}$$

$$\mathbf{G}_k = \frac{\partial \mathbf{g}(\mathbf{x}_k, \mathbf{n}_k)}{\partial \mathbf{x}_k} =$$
$$\begin{bmatrix} \frac{x}{\sqrt{\beta}} & \frac{y}{\sqrt{\beta}} & \frac{z}{\sqrt{\beta}} & 0 & 0 & 0 \\ \frac{-y}{x^2\gamma} & \frac{1}{x\gamma} & 0 & 0 & 0 & 0 \\ \frac{\dot{x}}{\sqrt{\beta}} - \frac{x\alpha}{\beta^{3/2}} & \frac{\dot{y}}{\sqrt{\beta}} - \frac{y\alpha}{\beta^{3/2}} & \frac{\dot{z}}{\sqrt{\beta}} - \frac{z\alpha}{\beta^{3/2}} & \frac{x}{\sqrt{\beta}} & \frac{y}{\sqrt{\beta}} & \frac{z}{\sqrt{\beta}} \\ -f_u y/x^2 & f_u/2 & 0 & 0 & 0 & 0 \\ -f_v z/x^2 & 0 & f_v/2 & 0 & 0 & 0 \end{bmatrix} \tag{25}$$

$$\mathbf{E} = \frac{\partial \mathbf{g}(\mathbf{x}_k, \mathbf{n}_k)}{\partial \mathbf{n}_k} = \begin{bmatrix} 1 & & & & \\ & 1 & & & \\ & & 1 & & \\ & & & 1 & \\ & & & & 1 \end{bmatrix} \tag{26}$$

$$\mathbf{n}' = \frac{\partial \mathbf{g}(\mathbf{x}_k, \mathbf{n}_k)}{\partial \mathbf{n}_k}\Big|_{\check{\mathbf{x}}_k, \mathbf{0}} \mathbf{n}_k \tag{27}$$

$$\mathbf{R}'_k = \mathbf{E}\mathbf{R}\mathbf{E}^T \tag{28}$$

In order to perform trajectory estimation, data association must be performed for both the camera and radar data-stream. Data association for camera data is performed through external association as cameras provide colour information which can be utilized to associate image data without input from the estimation algorithm. However, external association is not feasible for captured radar data as it does not provide unique features by which to associate data. Figure 2 shows all measurements that are returned within the field of view (FOV) considered. The Vicon ground truth measurements are shown in green and the closest radar measurement at each timestep are overlayed in red. It can be seen that periods of consistent and inconsistent radar data exist in the presence of many non-target measurements. To solve radar association, we employ a data association methodology involving EKF-based prediction, gating and euclidean distance association. At each timestep, a conservative gating region is established using the prediction of the EKF. Only measurements falling within the conservative gating region can be associated to the trajectory being estimated.

If multiple measurements fall within the gating region, the nearest neighbour based on euclidean distance is associated to the trajectory. If no radar measurement falls within the gating region, the state of the trajectory is propagated forward without a radar measurement.

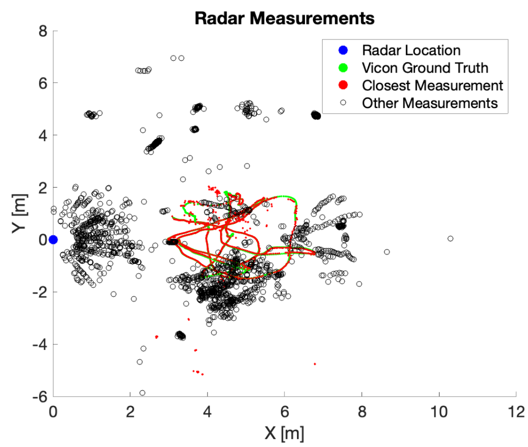

Fig. 2. Radar Measurements Projected in 2D Plane

It is inevitable that imperfections will occur in data association. For this reason, outlier rejection is vital to the performance of the estimation algorithm as outliers can cause an EKF to diverge. Recent work [9] utilizing dynamic saturation of the EKF innovation is implemented in this project. The dynamic nature of the saturation point allows for outliers in the innovation to be completely rejected. At the same time, if a large innovation produced is sustained the innovation saturation point will grow accordingly. In comparison, a static innovation threshold would not fully reject outliers as the outlier innovation would utilize the static threshold set. In addition, it would be slow to correct estimated states when the required innovation is greater than that of the static threshold. The saturated innovation for each radar measurement is defined as

$$\text{sat}_{\sigma}(\mathbf{y}_k - \mathbf{g}(\check{\mathbf{x}}_k, \mathbf{0})) = \begin{bmatrix} \text{sat}_{\sqrt{\sigma_R}}(\mathbf{y}_{R,k} - \mathbf{g}_R(\check{\mathbf{x}}_{R,k}, \mathbf{0})) \\ \text{sat}_{\sqrt{\sigma_A}}(\mathbf{y}_{A,k} - \mathbf{g}_A(\check{\mathbf{x}}_{A,k}, \mathbf{0})) \\ \text{sat}_{\sqrt{\sigma_{\dot{R}}}}(\mathbf{y}_{\dot{R},k} - \mathbf{g}_r(\check{\mathbf{x}}_{\dot{R},k}, \mathbf{0})) \end{bmatrix} \tag{29}$$

where

$$\text{sat}_{\sqrt{\sigma_\varepsilon}}(r) = \max\{-\varepsilon, \min\{\varepsilon, r\}\} \tag{30}$$

Equations 31 and 32 define the varying innovation saturation employed in this outlier rejection method for a given measurement i.

$$\dot{\sigma}_{i,k} = \lambda_{1,i}\sigma_{i,k} + \gamma_{1,i}\varepsilon_{i,k}e^{-\varepsilon_{i,k}} \tag{31}$$

$$\dot{\varepsilon}_{i,k} = \lambda_{2,i} + \gamma_{2,i}(\mathbf{y}_{i,k} - \mathbf{g}_i(\check{\mathbf{x}}_k, \mathbf{0})) \tag{32}$$

where $\sigma_{i,0} > 0$, $\varepsilon_{i,0} > 0$, $\lambda_{1,i}, \lambda_{2,i} < 0$ and $\gamma_{1,i}, \gamma_{2,i} > 0$.

Figure 3 shows the performance of the outlier rejection for results obtained using weak data association performance. Many outliers in the innovation are removed, but persistent increases in innovation allow for the innovation to increase. Final results shown in Figure 10 benefit less from outlier rejection due to the strong performance of the data association method applied.

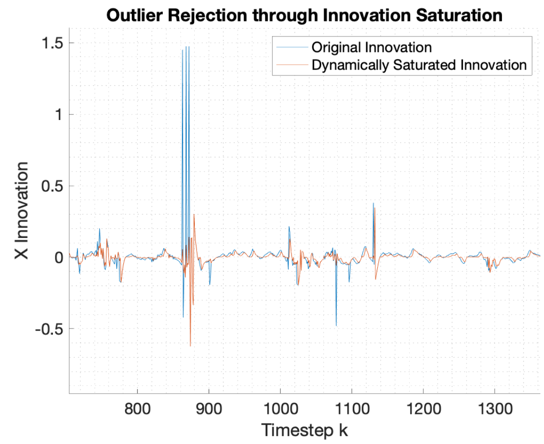

Fig. 3. Outlier Rejection

III. Results

A. Simulation Results

Confined Area Random Aerial Trajectory Emulator (CARATE) [10] is utilized to generate simulation trajectories iteratively based on previous trajectory history and a set of random variables. The position of the the UAV at time step n is determined using Equation 33 where ϕ'_n is the local azimuth angle and θ'_n is the local elevation angle.

$$x_n = x_{n+1} + T v_n \cos(\phi'_n)\sin(\theta'_n) \tag{33}$$

$$y_n = y_{n+1} + T v_n \sin(\phi'_n)\sin(\theta'_n) \tag{34}$$

$$z_n = z_{n+1} + T v_n \cos(\theta'_n) \tag{35}$$

where the values in the above equation depend on the previous state values in addition to a random component by

$$\theta'_n = \theta_{seed,n} + \delta\theta_n \tag{36}$$

$$\phi'_n = \phi_{seed,n} + \delta\phi_n \tag{37}$$

$$v_n = v_{seed,n} + \delta v_n \tag{38}$$

The distribution of the random component and the number of states in which the trajectory generation depends upon can be modified allowing for a variety of trajectory shapes to be evaluated. Figure 5 shows estimation error results obtained from the simulated trajectory in Figure 4.

B. Dataset

The experimental dataset collected, consists of data from the Continental ARS4-A 2D automotive radar system in addition to the ground truth location of the radar sensor and the target via the Vicon motion capture system. Although the Continental ARS4-A radar system only provides range and azimuth positional information, the characteristics of the emitted radar lobes allow for returns over a 16° elevation.

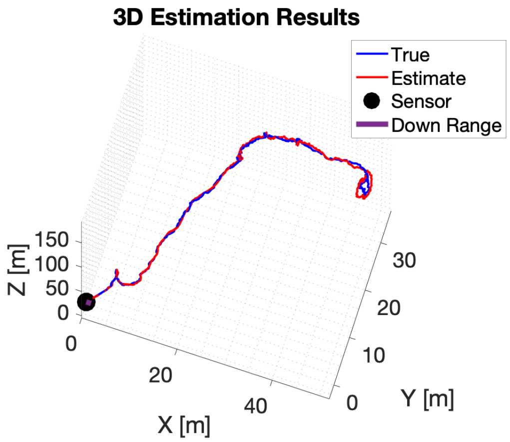

Fig. 4. Simulation 3D Estiamtion

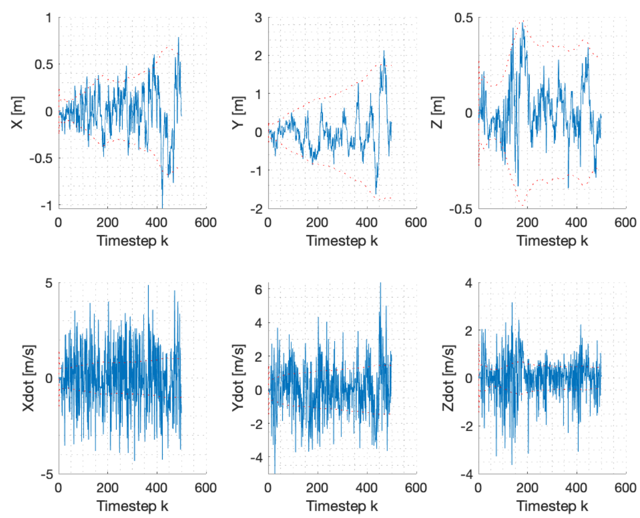

Fig. 5. Simulation Error Results

Vicon markers can be seen on the radar system and on the target in Figure 6. The target shown in Figure 6 is a reflective corner which produces a strong and consistent radar return signature.

Figure 2 shows all measurements returned by the radar system as well as measurements matched to the ground truth Vicon data using the ground truth data. Comparing the matched measurements in Figure 2 to the ground truth produces the measurement error plots shown in Figure 7 and Figure 8. Both measurements can be seen to have minimal biases. Although when running the trajectory estimation algorithm, ground truth data will not be available, we account for the biases present in the radar measurements as sensor biases are often determined through simple calibration methods. Also, apparent biases could simply be the result of error between the physical Vicon marker locations and the measured target location or radar "origin".

Due to prolonged issues with the integrated camera data collection, simulated camera data is added via the ground

Fig. 6. Sensor Suite and Target

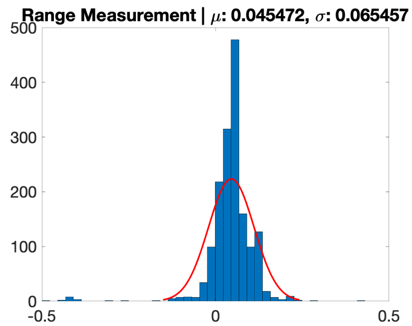

Fig. 7. Radar Range Measurement Error

truth data and measurement noise signature based on that found in the *Stary Night Dataset*. A focal length 450 pixels is utilized. Zero-mean gaussian noise with a standard deviation of 16 pixels is added to the pixel coordinates. This 16 pixel standard deviation is more measurement noise than what is present in the *Stary Night Dataset*. External data association will be assumed for the camera data. In an UAV tracking system this would be done through image processing to determine the target UAVs location in the image. For experimental methods similar to what is conducted in this project, an April tag could be placed on the front of the reflective radar target.

C. Experimental Results

Experimental results obtained from the EKF trajectory estimation system including data association and outlier rejection are shown in Figure 9 and Figure 10. Figure 9

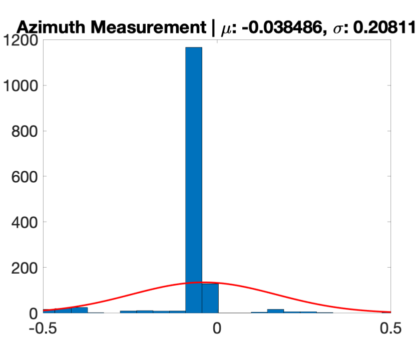

Fig. 8. Radar Azimuth Measurement Error

shows a 3D visualization of a portion of the estimated trajectory.

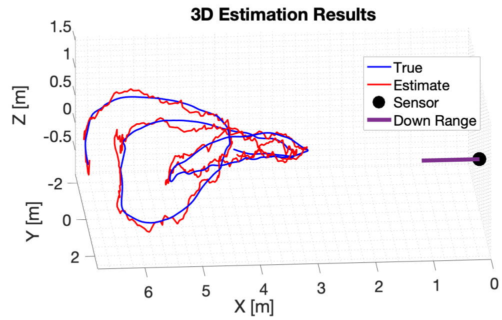

Fig. 9. 3D Trajectory Estimation

Figure 10 shows the error for the six estimated states in addition the $\pm 3\sigma$ bound for each state. The error can be seen to generally lie within the covariance bound with the exception of a significant point of error before timestep 200. This error is not the result of an outlier measurement and was therefore not removed. The error is caused by a sudden, unnatural movement during data collection. Current UAVs are not capable of sudden acceleration at that rate which was produced by the human controlled reflective radar target.

Various parameters were set in trajectory estimation solution. The scaling factor q of the motion noise is $1/7$, the observation covariance matrix utilizes variances provided by the radar unit for the range and range rate measurements. Azimuth variance provided by the radar unit was orders of magnitude more confident than the data-sheet specification and caused the estimation to diverge. For this reason, the variance for the azimuth was set to 0.02 rad in alignment with the radar specifications. The pixel variance in the observation covariance matrix was set to 16^2 for both camera measurements in alignment with the noise added to the camera measurements.

IV. Discussion and Conclusion

Overall, this work provides insight into the ability of a 2D automotive radar in trajectory estimation of an object in 3D space such as a UAV. It is demonstrated that for sufficiently dense radar data, trajectory can be effectively estimated through data association, outlier rejection and state estimation. The cost effectiveness of this solution makes it worth exploring further.

Current limitations do exist in cases in which data is absent for extended periods of time, significant noise is present and the trajectory of the target changes abruptly. Radar return measurements from UAVs will likely be significantly weaker that those from the reflective radar target used in this work. This reduction in signal strength may cause the returned data to not be consistent enough for the estimation method to converge to the correct solution. Second, trajectory estimation was evaluated within a short range lab environment. Although the Continental ARS4-A specification states ranges up to 250m, the impact of increase in range would also need to be investigated for a complete solution.

There are multiple potential extensions for future work in relation to this project. Much work exists in extending experimental testing to different cases that would be encountered if this solution were to be implemented for UAV trajectory estimation. The main area to be tested further is the ability of the radar system to provide consistent returns from a UAV instead of the reflective radar target used in this project. In addition to further experimental testing, other trajectory estimation, data association and outlier rejection methodologies could be investigated. For example, the UKF may provide improved estimation results. Data association is critical to the success of this method as the radar system produces a significant number of false positive measurements. Therefore, it would be beneficial to investigate the impact of more advanced data association methods such as probabilistic data association (PDA) or multiple hypothesis tracking (MHT).

Appendix

A. Fisher Information Matrix: Radar Only System

The Fisher Information Matrix (FIM) is defined according to Equation 39 where θ are the states being estimated, $h()$ is the observation model and $\mathbf{R}$ is the invertible covariance matrix.

$$\mathbf{F}_{\theta}(X) = \nabla_{\theta} h(\theta) \mathbf{R}^{-1} \nabla_{\theta}^{T} h(\theta) \tag{39}$$

For the radar only system with the observation model defined as 40 the measurements are independent of each other. Therefore an identity matrix can be used as the covariance matrix.

$$\begin{bmatrix} R_k \\ A_k \\ \dot{R}_k \end{bmatrix}_{(\mathbf{y}_k)} = \begin{bmatrix} \sqrt{[x_k, y_k, z_k][x_k, y_k, z_k]} \\ \arctan(\frac{y_k}{x_k}) \\ \frac{[x_k, y_k, z_k][\dot{x}_k, \dot{y}_k, \dot{z}_k]^T}{\sqrt{[x_k, y_k, z_k][x_k, y_k, z_k]}} \end{bmatrix} + \mathbf{n}_k \tag{40}$$

The components needed to build the FIM will thus be (subscripts k have been removed),

$$\mathbf{R} = \mathbf{I}_{(3\times3)} \tag{41}$$

$$\nabla_{\theta}^{T} h(\theta) = \begin{bmatrix} \frac{x}{\sqrt{\beta}} & \frac{y}{x^2\gamma} & \frac{\dot{x}}{\sqrt{\beta}} - \frac{x\alpha}{\beta^{3/2}} \\ \frac{y}{\sqrt{\beta}} & \frac{1}{x\gamma} & \frac{\dot{y}}{\sqrt{\beta}} - \frac{y\alpha}{\beta^{3/2}} \\ \frac{z}{\sqrt{\beta}} & 0 & \frac{\dot{z}}{\sqrt{\beta}} - \frac{z\alpha}{\beta^{3/2}} \\ 0 & 0 & \frac{x}{\sqrt{\beta}} \\ 0 & 0 & \frac{y}{\sqrt{\beta}} \\ 0 & 0 & \frac{z}{\sqrt{\beta}} \end{bmatrix} \tag{42}$$

where

$$\alpha = [x, y, z][\dot{x}, \dot{y}, \dot{z}]^T \tag{43}$$

$$\beta = x^2 + y^2 + z^2 \tag{44}$$

$$\gamma = \frac{y^2}{x^2} + 1 \tag{45}$$

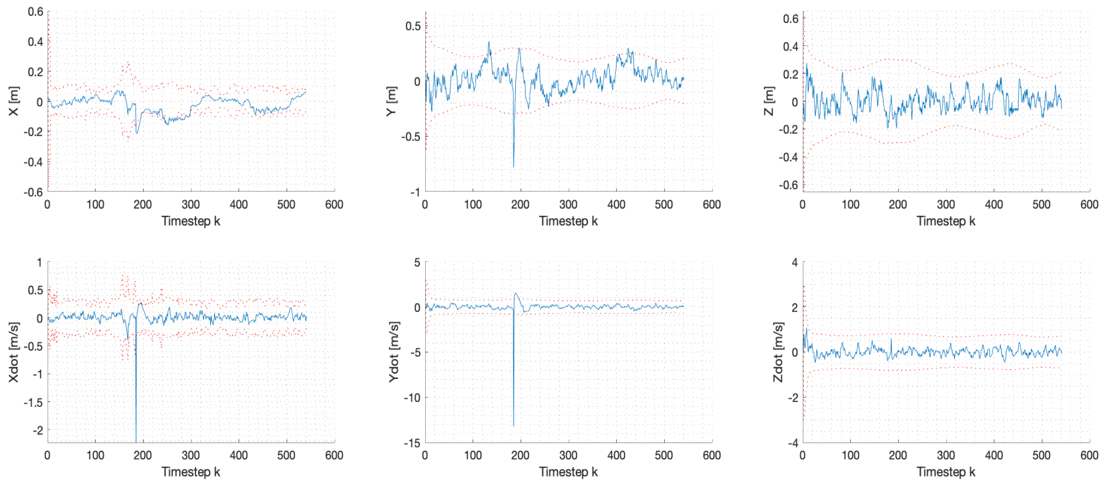

Fig. 10. Estimation Error Results with 3σ Bounds

From these components the FIM is (using α, β, γ)

$$\mathbf{F}_\theta(X) = \begin{bmatrix} \psi^2 + \frac{x^2}{\beta} + \frac{y^2}{x^4\sqrt{\gamma}} & \eta & \lambda & \frac{x\psi}{\sqrt{\beta}} & \frac{y\psi}{\sqrt{\beta}} & \frac{x\psi}{\sqrt{\beta}} \\ \eta & \frac{1}{x^2\gamma^2} + \omega^2 + \frac{y^2}{\beta} & \varepsilon & \frac{x\omega}{\sqrt{\beta}} & \frac{y\tau}{\sqrt{\beta}} & \frac{z\omega}{\sqrt{\beta}} \\ \lambda & \varepsilon & \tau^2 + \frac{z^2}{\beta} & 12 & 9 & 6 \\ \frac{x\psi}{\sqrt{\beta}} & \frac{x\omega}{\sqrt{\beta}} & \frac{x\tau}{\sqrt{\beta}} & \frac{x^2}{\beta} & \frac{xy}{\beta} & \frac{xz}{\beta} \\ \frac{y\psi}{\sqrt{\beta}} & \frac{y\omega}{\sqrt{\beta}} & \frac{y\tau}{\sqrt{\beta}} & \frac{xy}{\beta} & \frac{y^2}{\beta} & \frac{yz}{\beta} \\ \frac{z\psi}{\sqrt{\beta}} & \frac{z\omega}{\sqrt{\beta}} & \frac{z\tau}{\sqrt{\beta}} & \frac{xz}{\beta} & \frac{yz}{\beta} & \frac{z^2}{\beta} \end{bmatrix} \tag{46}$$

where

$$\eta = \psi\omega - \frac{y}{x^3\gamma^2} + \frac{xy}{\beta} \tag{47}$$

$$\varepsilon = \omega\tau + \frac{yz}{\beta} \tag{48}$$

$$\lambda = \psi\tau + \frac{xz}{\beta} \tag{49}$$

$$\psi = \frac{\dot{x}}{\sqrt{(\tau)}} - \frac{x\alpha}{\beta^{3/2}} \tag{50}$$

$$\omega = \frac{\dot{y}}{\sqrt{(\tau)}} - \frac{y\alpha}{\beta^{3/2}} \tag{51}$$

$$\tau = \frac{\dot{z}}{\sqrt{(\tau)}} - \frac{z\alpha}{\beta^{3/2}} \tag{52}$$

The FIM in reduced row echelon form is

$$\mathbf{F}_\theta(X) = \begin{bmatrix} 1 & 0 & 0 & -\frac{x^2z}{c} & b & -\frac{xz^2}{c} \\ 0 & 1 & 0 & b & -\frac{y^2z}{c} & -\frac{yz^2}{c} \\ 0 & 0 & 1 & \frac{xa}{c} & \frac{ya}{c} & \frac{za}{c} \\ 0 & 0 & 0 & 0 & 0 & 0 \\ 0 & 0 & 0 & 0 & 0 & 0 \\ 0 & 0 & 0 & 0 & 0 & 0 \end{bmatrix} \tag{53}$$

where

$$a = x^2 + y^2 \tag{54}$$

$$b = -\frac{xyz}{c} \tag{55}$$

$$c = [x^2, y^2, z^2][\dot{x}, \dot{y}, \dot{z}]^T \tag{56}$$

It can be seen that the matrix is not full rank meaning the system is unobservable.

B. Fisher Information Matrix: Radar and Camera System

Following the same procedure of Section IV-A, the FIM in reduced row echelon form for the model in Equation 57 is shown in Equation 58.

$$\underbrace{\begin{bmatrix} R_k \\ A_k \\ \dot{R}_k \\ u_k \\ v_k \end{bmatrix}}_{(\mathbf{y}_k)} = \begin{bmatrix} \sqrt{[x_k, y_k, z_k][x_k, y_k, z_k]} \\ \arctan(\frac{y_k}{x_k}) \\ \frac{[x_k, y_k, z_k][\dot{x}_k, \dot{y}_k, \dot{z}_k]^T}{\sqrt{[x_k, y_k, z_k][x_k, y_k, z_k]}} \\ f_u y_k / x_k \\ f_v z_k / x_k \end{bmatrix} + \mathbf{n}_k \tag{57}$$

$$\begin{bmatrix} 1 & 0 & 0 & 0 & 0 & 0 \\ 0 & 1 & 0 & 0 & 0 & 0 \\ 0 & 0 & 1 & 0 & 0 & 0 \\ 0 & 0 & 0 & 1 & \frac{y}{z} & \frac{z}{x} \\ 0 & 0 & 0 & 0 & 0 & 0 \\ 0 & 0 & 0 & 0 & 0 & 0 \end{bmatrix} \tag{58}$$

It can be seen that the matrix is not full rank meaning the system is not observable.

C. Fisher Information Matrix: Radar and Camera System Without Velocity Estimation

Following the same procedure of Section IV-A, the FIM in reduced row echelon form for the model in Equation 59 is shown in Equation 60. Note that the difference between this proof and than of Section IV-B is that only the three positional states are now being estimated as the three velocity states have been removed.

$$\begin{bmatrix} R_k \\ A_k \\ u_k \\ v_k \end{bmatrix}_{(\mathbf{y}_k)} = \begin{bmatrix} \sqrt{[x_k, y_k, z_k][x_k, y_k, z_k]} \\ \arctan(\frac{y_k}{x_k}) \\ f_u y_k / x_k \\ f_v z_k / x_k \end{bmatrix} + \mathbf{n}_k \tag{59}$$

$$\begin{bmatrix} 1 & 0 & 0 \\ 0 & 1 & 0 \\ 0 & 0 & 1 \end{bmatrix} \tag{60}$$

It can be seen that the matrix is full rank meaning the system is observable.

D. Radar-Camera Locally Weakly Observable

The system radar-camera system with the measurement model defined in Equation 57 can be shown to be locally weakly observable through the construction of an observability matrix from the gradients of the the Lie derivatives of our non-linear measurement model $\mathbf{h}()$ [7][8].

$$L^0 h_k = h_k \tag{61}$$

$$L^1_{f_j} h_k = \nabla_{\mathbf{x}} h_k f_j \tag{62}$$

where $L^1_{f_j}$ is the first Lie derivative

$$f_j = \dot{\mathbf{x}} = \begin{bmatrix} \dot{x} \\ \dot{y} \\ \dot{z} \\ 0 \\ 0 \\ 0 \end{bmatrix} \tag{63}$$

Locally weak observability is proven by showing that the following chosen observability matrix is full rank:

$$\mathbf{O} = \begin{bmatrix} \nabla_{\mathbf{x}} L^0 h_k \\ \nabla_{\mathbf{x}} L^1_{f_j} h_k \end{bmatrix} \tag{64}$$

The matrix $\mathbf{O}$ is placed in its reduced row echelon form using Gauss-Jordan elimination.

$$\mathbf{O} = \begin{bmatrix} 1 & 0 & 0 & 0 & 0 & 0 \\ 0 & 1 & 0 & 0 & 0 & 0 \\ 0 & 0 & 1 & 0 & 0 & 0 \\ 0 & 0 & 0 & 1 & 0 & 0 \\ 0 & 0 & 0 & 0 & 1 & 0 \\ 0 & 0 & 0 & 0 & 0 & 1 \\ 0 & 0 & 0 & 0 & 0 & 0 \\ 0 & 0 & 0 & 0 & 0 & 0 \\ 0 & 0 & 0 & 0 & 0 & 0 \\ 0 & 0 & 0 & 0 & 0 & 0 \end{bmatrix} \tag{65}$$

Since the observability matrix has a rank of six and there are six estimated states, the camera-radar system is locally, weakly observable.

References

[1] P. Nguyen, H. Truong, M. Ravindranathan, A. Nguyen, R. Han, and T. Vu, "Matthan: Drone presence detection by identifying physical signatures in the drone's rf communication," in *Proceedings of the 15th Annual International Conference on Mobile Systems, Applications, and Services*. ACM, 2017, pp. 211–224.

[2] A. Rozantsev, S. N. Sinha, D. Dey, and P. Fua, "Flight dynamics-based recovery of a uav trajectory using ground cameras," in *Proceedings of the IEEE Conference on Computer Vision and Pattern Recognition*, 2017, pp. 6030–6039.

[3] B. Kim, D. Khan, C. Bohak, W. Choi, H. Lee, and M. Kim, "V-rbnn based small drone detection in augmented datasets for 3d ladar system," *Sensors*, vol. 18, no. 11, p. 3825, 2018.

[4] S. J. Julier and J. K. Uhlmann, "Unscented filtering and nonlinear estimation," *Proceedings of the IEEE*, vol. 92, no. 3, pp. 401–422, 2004.

[5] T. D. Barfoot, *State Estimation for Robotics*. Cambridge University Press, 2017.

[6] C. Jauffret, "Observability and fisher information matrix in nonlinear regression," *IEEE Transactions on Aerospace and Electronic Systems*, vol. 43, no. 2, pp. 756–759, 2007.

[7] J. Kelly and G. S. Sukhatme, "Visual-inertial sensor fusion: Localization, mapping and sensor-to-sensor self-calibration," *The International Journal of Robotics Research*, vol. 30, no. 1, pp. 56–79, 2011.

[8] R. Hermann and A. Krener, "Nonlinear controllability and observability," *IEEE Transactions on automatic control*, vol. 22, no. 5, pp. 728–740, 1977.

[9] H. Fang, M. A. Haile, and Y. Wang, "Robust extended kalman filtering for systems with measurement outliers," *arXiv preprint arXiv:1904.00335*, 2019.

[10] A. Papaiz and A. M. Tonello, "Azimuth and elevation dynamic tracking of uavs via 3-axial ula and particle filtering," *International Journal of Aerospace Engineering*, vol. 2016, 2016.